


Article

Conceptual Design and Dynamic Analysis of a Wind–Wave Energy Converter with a Mass-Adjustable Buoy

Yifeng Shi ^{1,2}, Jiahuan Lin ^{1,2}, Zexin Zhuge ^{1,2}, Rongye Zheng ^{1,2,*} and Jun Zhang ^{1,2,*} 

¹ Fuzhou Institute of Oceanography, Fuzhou 350108, China; yifeng_shi@foxmail.com (Y.S.); fzulinjiahuan@foxmail.com (J.L.); zhugezexin@foxmail.com (Z.Z.)

² School of Mechanical Engineering and Automation, Fuzhou University, Fuzhou 350108, China

* Correspondence: ryzheng@fzu.edu.cn (R.Z.); zhang_jun@fzu.edu.cn (J.Z.)

Abstract: To reduce the levelized cost of energy (LCOE) for offshore wind turbines, a novel wind–wave energy converter (WVEC) with a mass-adjustable buoy is designed. To analyze the impact of buoy mass variations on the system, a coupled comprehensive numerical model is established to simulate the aerodynamics of the turbine and the hydrodynamics of the platform and buoy. It is found that the occurrence of the buoy out of water significantly reduces the output power. Adjusting the buoy’s mass with suitable strategy can prevent the impact of slamming loads and improve the power output. The mass adjustment strategy is determined based on the output power of the wave energy converter under regular wave conditions. It is found that the mass adjustment strategy can significantly enhance the output power of combined system. The buoy does not move out of the water under the extreme conditions, which avoids the impact of slamming loads on system stability. Moreover, mass-adjustable buoys can reduce the risk of mooring line failure compare to a wind turbine without a buoy.

Keywords: wind–wave energy converter; mass-adjustable buoy; power optimization; conceptual design



Citation: Shi, Y.; Lin, J.; Zhuge, Z.; Zheng, R.; Zhang, J. Conceptual Design and Dynamic Analysis of a Wind–Wave Energy Converter with a Mass-Adjustable Buoy. *J. Mar. Sci. Eng.* **2024**, *12*, 1460. <https://doi.org/10.3390/jmse12081460>

Academic Editors: Eugen Rusu, Kostas Belibassakis and George Lavidas

Received: 30 July 2024

Revised: 20 August 2024

Accepted: 21 August 2024

Published: 22 August 2024



Copyright: © 2024 by the authors. Licensee MDPI, Basel, Switzerland. This article is an open access article distributed under the terms and conditions of the Creative Commons Attribution (CC BY) license (<https://creativecommons.org/licenses/by/4.0/>).

1. Introduction

With the development of wind power technology, the global weighted LCOE for offshore wind power has decreased from 0.127 USD/kWh in 2018 to 0.074 USD/kWh in 2023 with a reduction of approximately 42%. However, the rate of cost reduction is gradually slowing down, and there still exists a gap between the LCOE of offshore wind power and onshore wind power (0.042 USD/kWh). Meanwhile, ocean wave energy has attracted increasing attention because of its high availability and low environmental impact as a high-power-density marine renewable energy source [1,2]. But it has seen a relatively slow development; the primary reason for this slow progress is the high costs associated with site permits, transmission lines, and mooring systems [3]. Attaching a wave energy converter (WEC) to the platform of offshore wind turbines addresses this issue, accelerates WEC development, and provides a promising avenue for further reducing the LCOE of offshore wind turbines [4–11].

Following this train of thought, various types of combined system were proposed. The earliest research can be dated back to the 2010s. The MARINA project, initially funded by the European Union, introduced the concept of a spar–torus combination (STC), which combines a spar-type floating wind turbine with a torus-shaped structure to form a WVEC [12]. WVECs based on semi-submersible platforms have gained more attention due to its convenience in installation and flexibility in deployment [13]. Michailides et al. designed a WVEC consisting of a semi-submersible wind turbine and three flap-style WECs, studying the impact of platform motion with different degrees of freedom on power generation [14]. Da Silva et al. designed a WVEC comprising a semi-submersible platform

and three spherical point absorber wave energy converters, investigating the wave energy absorption and motion characteristics of the hybrid system [15]. Homayoun et al. utilized the configuration features of unsupported semi-submersible platforms, installing a torus-shaped buoy on each of the three columns and studying the impact of power take-off (PTO) system parameters on power output through simulations [16]. From these studies, it is evident that, given the structural characteristics of semi-submersible platforms, they can be combined with a wider variety and quantity of WECs. However, compared to spar-type platforms, maintaining system stability with semi-submersible platforms is more difficult. Haji's research found that the combination of floating wind turbines and point absorber wave energy converters increases platform yaw and heave motion, and the impact of WECs on the bending stress at the base of the wind turbine tower affects the turbine's lifespan [17]. In this view, it is essential to consider the influence of WECs on the platform and not focus solely on power output in designing WWECs.

To further enhance the power output of the system, efforts should be made to maximize the individual WEC's power output. Currently, the optimization of WECs has primarily focused on the buoy shape and PTO system parameters [18]. Enhancing the capture width of WECs through active control can further increase the system's power output. Liu et al. applied latching control to a raft-type WEC with multiple DOFs, resulting in an enhancement of up to 10.54% in power [19]. Hillis et al. designed optimal buoy motion trajectories based on wave conditions, modulating the buoy's motion by varying the stiffness and damping coefficients of the PTO system [20]. Simulation results indicated that the active control system, compared to its passive counterpart, contributed to a power increase of over 80%. Fang et al. studied the method of adjusting the buoy mass to match the resonance frequency of the waves to improve the output power of the wave energy converter [21]. However, existing WECs with active control strategies fail to account for the mutual influence between the WEC and the wind turbine. Considering the overall economic viability [22], WECs should not compromise the lifespan of the wind turbines. Many control strategies are not suitable for WWEC. For integrated wind and wave energy systems, the operation of the buoy must also consider the stability of the wind turbine. To ensure the smooth operation of turbines, WECs are typically constrained, and in extreme conditions, buoys are often locked and submerged [23]. Researchers conducted experiments to study the operation of wind-wave energy systems under extreme conditions. Nonlinear loads resulting from buoy surfacing and submerging could potentially cause significant harm. Locking and submerging the buoy effectively reduced the occurrence of this phenomenon [24–27]. While this approach ensures system safety, it results in wasted wave energy and reduced wave energy capture width for WECs.

Based on the operational characteristics of WWEC with point absorber WECs, this paper proposes a WWEC with a mass-adjustable buoy. By adjusting the draft of the buoy, the impact of bottom slamming loads on the WWEC is mitigated. This approach provides a solution to the issue of the WEC in WWECs failing to operate properly under extreme conditions, while also moderately improving the output power of the WEC under normal conditions.

In the present paper, we designed a novel WWEC with a mass-adjustable buoy for the NREL-5MW wind turbine. In Section 2, the mass adjustment mechanism is designed. In Section 3, a coupled numerical model is established and the accuracy of the model is verified. In Section 4, a mass adjustment strategy is designed, and the power output and dynamic response of the system are analyzed under eight environmental conditions to validate the feasibility and safety of the system. Finally, conclusions are drawn in Section 5.

2. Wind-Wave Energy Converter Design

2.1. Connections between the Platform and the Buoy

This paper designs the WWEC based on the torus-shaped buoy, and the connection between the buoy and the platform column is referenced from the STC system, as shown in Figure 1a. Four connecting rods are used to connect the buoy with the column, which

mainly restricts the relative motion of the two bodies in pitch, yaw, and roll directions. Considering the reliability of the connecting rods, the guide-roller system is used to assist in restricting the relative motion of the two bodies in the surge and sway directions. End stop springs are used to limit the relative motion of the buoy and the platform in the heave direction, its main function is to prevent excessive relative displacement in extreme conditions. Wave energy is harnessed through the relative heave motion between the buoy and the platform and subsequently converted into electrical energy via the PTO system.

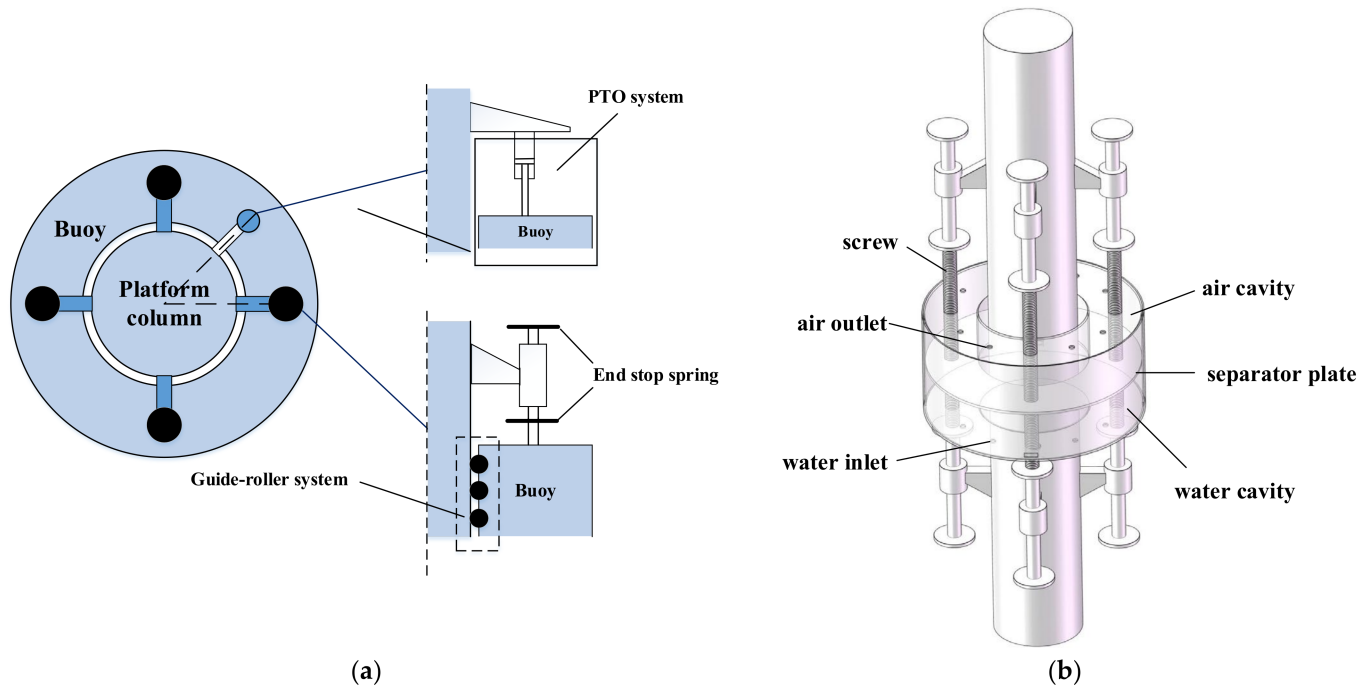


Figure 1. Wave energy converter (a) simplified diagram of the connection section; (b) structure of mass adjustment.

2.2. Buoy Structure Design

A mass adjustment structure based on the torus-shaped buoy is designed; it alters the buoy’s mass by adjusting the internal ballast water. The specific structure of the mass-adjustable buoy is shown in Figure 1b. The conceptual design of the mass adjustment structure for the buoy is based on the connection system. The middle section of the connecting rod, which attaches the buoy to the platform, is designed with the thread that runs through the entire buoy. The interior of the buoy is hollow and partitioned into two sections by a separator plate: an air cavity and a water cavity. The connecting rod and separator plate are connected by threads. Several small openings are located on both the upper and lower surfaces of the buoy to permit the circulation of seawater and air. The rod and the separator plate are connected through threading. By rotating the four rods, the plate’s position is controlled, to adjust the height of the water chamber for the desired buoy mass. The connecting rod rotates to move the separator plate upward, allowing seawater to enter through the small openings at the bottom and air to escape from the top, thus increasing the mass as more seawater fills the buoy. Conversely, the connecting rod moves the separator plate downward, causing seawater to exit through the small openings at the bottom, thereby reducing the mass of the buoy.

2.3. Floating Wind Turbine

The schematic diagram of the WWEC is shown in Figure 2. The origin of the global coordinate system is at point O, where the center of the tower intersects with the sea surface. This paper selects the NREL-5MW wind turbine as the component for the WWEC, due to its structural simplicity, modelling suitability, and commercial viability [28], and it

provides easy access for subsequent validation. The platform uses the braceless steel semi-submersible platform proposed in [29], with a design water depth of 200 m. Compared to the OC4-Semi platform configuration proposed by NREL, the braceless steel structure platform provides more heave motion space for the buoy, which is more conducive to the buoy's wave energy absorption. The external dimensions of the buoy are based on the integrated wind and wave energy system researched in [27]. The conceptual drawing of the platform with the buoy is shown in Figure 3. The base of the tower is coincident with the top of platform and is located at an elevation of 10 m above the still water level (SWL). Main design parameters of the combined system are given in Table 1.

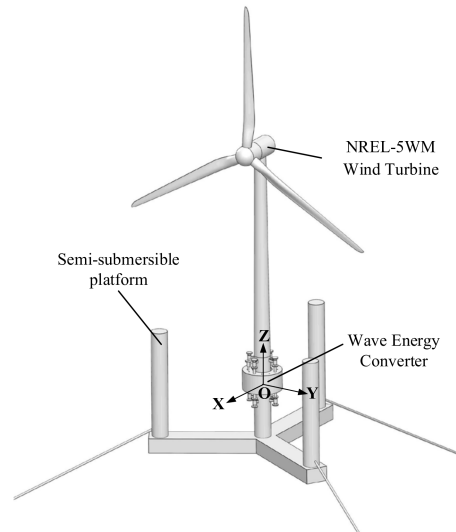


Figure 2. The schematic diagram of the WWEC.

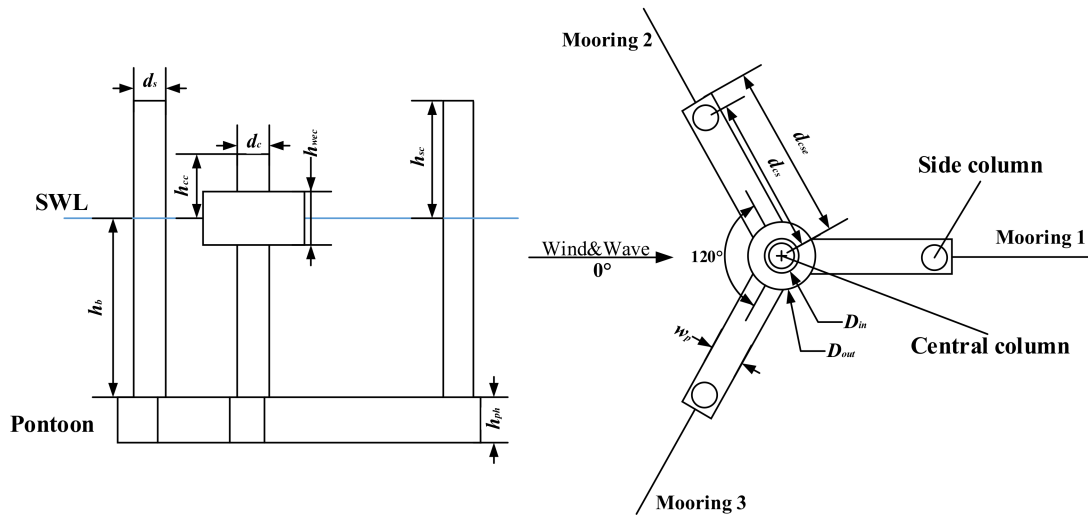


Figure 3. Conceptual drawings of the platform and buoy.

Table 1 does not provide the draft of the buoys, because the draft of the buoys varies with changes in mass. To ensure the reliability of the adjustment system and avoid frequent modifications, this study introduces only four adjustment settings, focusing on buoy drafts ranging from 1 to 4 m. Subsequently, further exploration will be conducted to determine whether buoys with larger masses are required. The main characteristic parameters of the buoy at different draft are presented in Table 2. To facilitate the description, draft of buoys is used to represent variations in the buoy's mass in the subsequent sections of the paper.

Table 1. Main design parameters of the combined system.

Property	Value
Wind turbine (NREL-5MW)	
Rotor–nacelle assembly mass	350 t
Tower mass	347.6 t
Center of gravity	(0.2 m, 0, 74 m)
Platform	
Central column diameter (d_c)	6.5 m
Side columns diameter (d_s)	6.5 m
Central column height, top to SWL (h_{cc})	10.0 m
Side columns height, top to SWL (h_{sc})	20.0 m
Columns draft, SWL to bottom (h_b)	24.0 m
Pontoon height (h_{ph})	6.0 m
Pontoon width (w_p)	9.0 m
Distance from central column to side columns (d_{cs})	41.0 m
Distance from central column center to pontoons edge (d_{cse})	45.5 m
Center of gravity	(0, 0, −24.36 m)
Mass	9738 t
Buoy	
Outer diameter (D_{out})	16.0 m
Inner diameter (D_{in})	8.0 m
Buoy height (h_{wec})	8.0 m

Table 2. Main characteristic parameters of the buoy at different draft.

Draft (m)	1	2	3	4
Mass (kg)	154,566	309,132	463,699	618,265
I_{xx}/I_{yy} (kgm ²)	5,775,860	10,547,039	14,545,387	18,002,752
I_{zz} (kgm ²)	6,116,137	12,232,275	18,348,412	24,464,550

The mooring system consists of three mooring lines whose distribution is illustrated in Figure 3. In this paper, the location of operation is considered in the northern North Sea. The design water depth of the WWEC is 200 m. Detailed design parameters of a mooring line are presented in Table 3.

Table 3. Design parameters of a single mooring line.

Mooring System	Value
Mass per unit length (in the air)	115 kg/m
Pretension at the fairlead	1.7×10^6 N
Un-stretched mooring line length	1073 m
Diameter of the mooring line length cross-section	0.137 m
Clump weight in water	1.5×10^4 kg
Distance from the attachment point of the clump weight to the fairlead	240 m

3. Coupled Numerical Model and Verification

3.1. Fully Coupled Numerical Model

FAST is a well-known tool used to calculate the aerodynamic loads and predict the dynamic response of floating wind turbines. AQWA is a commonly used commercial tool capable of performing time-domain and frequency-domain analyses on single or multiple floating structures, which has strong capabilities in calculating the nonlinear

dynamics of mooring lines. The baseline version of AQWA is incapable of predicting aerodynamic load and structural responses of floating wind turbine, while FAST cannot account for the interaction between multiple floating bodies and simplifies the influence of the mooring system. To accurately calculate the dynamic response of the WWEC under complex operating conditions, this paper employs the F2A tool developed by Yang et al. [30]. The flow chart of F2A is shown in Figure 4.

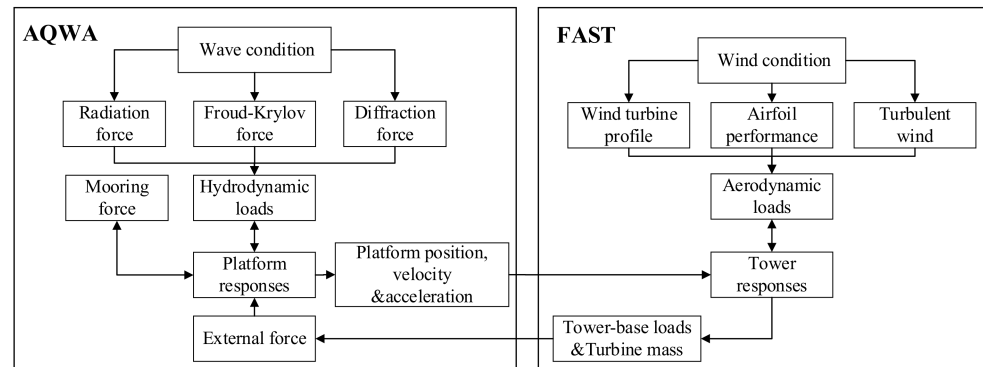


Figure 4. Flow chart of F2A.

F2A integrates the capabilities of FAST into AQWA via the user force module. It combines the wind turbine model established in FAST with the mooring system and the floating structure model in AQWA. F2A considers the effects of platform motion on the wind turbine and conveys the tower base loads calculated in FAST as external forces into AQWA. AQWA undertakes time-domain analysis to solve the motion equations [31]:

$$(M + m)\ddot{X}(t) + \int_0^t h(t - \tau)\dot{X}(\tau)d\tau + KX(t) = F(t) \tag{1}$$

$$M = \begin{pmatrix} M & 0 & 0 & 0 & Mz_G & -My_G \\ 0 & M & 0 & -Mz_G & 0 & Mx_G \\ 0 & 0 & M & My_G & -Mx_G & 0 \\ 0 & -Mz_G & My_G & I_{xx} & I_{xy} & I_{xz} \\ Mz_G & 0 & -Mx_G & I_{yx} & I_{yy} & I_{yz} \\ -My_G & Mx_G & 0 & I_{zx} & I_{zy} & I_{zz} \end{pmatrix} \tag{2}$$

where M is the mass matrix, M is the mass of the floating body, I_{ij} is the moment of inertia, (x_G, y_G, z_G) is the location of the center of gravity, m is the added mass matrix. K is the matrix for hydrostatic restoring forces. $X(t)$ is the displacement for the floating body, $F(t)$ is the total external force matrix, accounting for both hydrodynamic and aerodynamic forces, $h(t)$ is the velocity impulse function matrix. The velocity impulse matrix is derived from the radiation damping using Fourier transformation.

After completing the time-domain analysis in AQWA, F2A inputs the platform motion displacement, velocity, and acceleration from AQWA into FAST, after coordinating transformation, to correct the response of the wind turbine tower.

3.2. Hydrodynamic and Aerodynamic Loads

The model of the buoy and platform is created in AQWA to calculate the wave loads on both the platform and the torus-shaped buoy. Depending on the size of the structure, the characteristics of the wave load can vary significantly. For large-scale structures, the presence of the structure has a significant effect on the wave field. The diffraction and inertia load from waves are the main components. For small-scale structures, the viscous and inertial loads from the waves are the primary components. The platform of floating wind turbines is usually encompassing both types of structures.

The wind turbine model is established in FAST, and the aerodynamic loads on the wind turbine are calculated using the blade element momentum (BEM) theory [32]. BEM

assumes that the blade is composed of countless independent blade elements. Based on the blade model, the lift coefficient and drag coefficient of each blade element are determined. Then, the forces on each blade element are calculated according to the inflow wind speed and inflow angle. The thrust T and torque M on each blade element can be expressed as [30]:

$$dT = \frac{1}{2} \rho V^2 c (C_l \cos \varphi + C_d \sin \varphi) dr \tag{3}$$

$$dM = \frac{1}{2} \rho V^2 c (C_l \sin \varphi + C_d \cos \varphi) r dr \tag{4}$$

where ρ is the air density, V represents the relative velocity between the blade element and the air, c is the chord length of the blade element, C_l and C_d are the lift and drag coefficients of the blade element, respectively, and φ is the inflow angle. Using the above equations, the thrust and torque of each blade element are obtained. By integrating along the blade, the total aerodynamic load acting on the entire blade is calculated, leading to the determination of the rotor thrust. It is worth noting that the aerodynamic loads are also influenced by factors like the tower’s elastic deformation and the pitch system servo control. More detailed information on these factors can be found in the FAST documentation [33].

3.3. Hydrodynamic Coefficient

In a flow field, apart from the direct interaction through connection section, there exists hydrodynamic interaction between the semi-submersible and the buoy. The consideration of multi-body hydrodynamic coupling affects the calculation of added mass and radiation damping. This paper primarily focuses on the dynamic response of buoys in the heave direction, calculating the added mass and radiation damping in the heave direction for mass-adjustable buoys under the conditions of with and without hydrodynamic interaction, as shown in Figures 5 and 6.

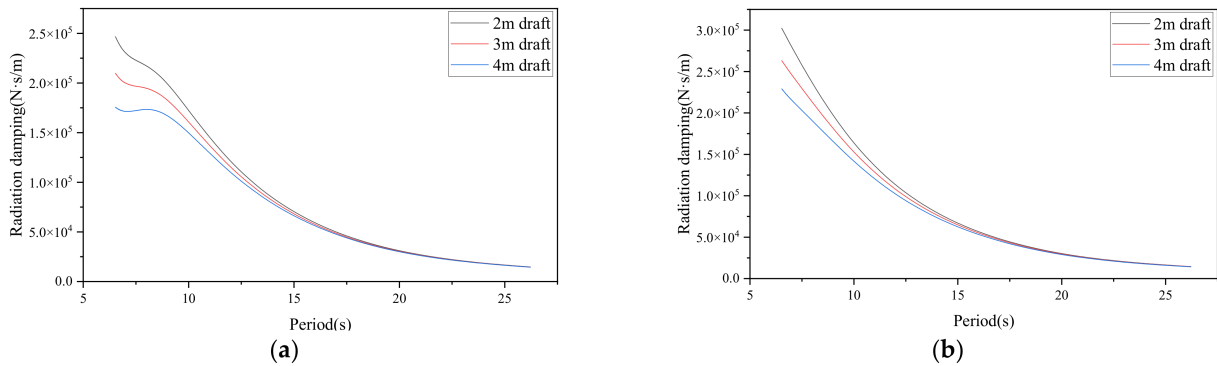


Figure 5. Radiation damping of the mass-adjustable buoy (a) with hydrodynamic interaction; (b) without hydrodynamic interaction.

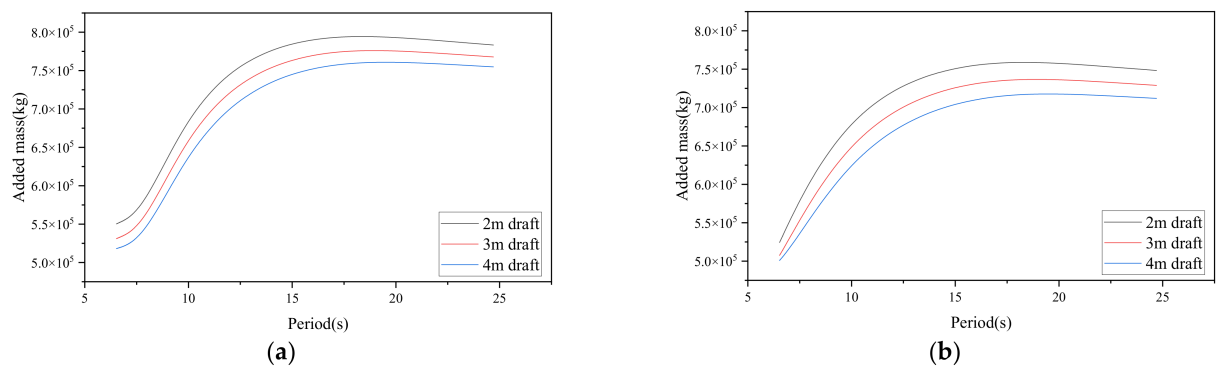


Figure 6. Added mass of the mass-adjustable buoy (a) with hydrodynamic interaction; (b) without hydrodynamic interaction.

From Figure 5, it can be observed that in both scenarios, the radiation damping decreases gradually as the wave period increases, with the overall trend being consistent. The influence of the buoy mass on radiation damping is also quite similar. As the mass decreases, radiation damping slightly increases at shorter periods. Figure 6 shows that the trends of added mass with respect to wave period and buoy mass are consistent in both scenarios. The mean error in added mass due to hydrodynamic interactions for the three buoy is 13,617 kg, 17,451 kg, and 19,603 kg, the mean error in radiation damping is 8823 Ns/m, 8381 Ns/m, and 7706 Ns/m.

Since this study need to investigate the impact of changes in buoy mass on its water entry and exit, a time-domain analysis of the system is required. However, real-time analysis of hydrodynamic interactions based on the relative motion between the platform and the buoy is extremely challenging. Considering that hydrodynamic interaction does not significantly alter the trend of hydrodynamic coefficients with respect to buoy mass and wave period, and that the errors in the added mass and radiation damping due to hydrodynamic interactions are relatively small compared to the buoy mass and the PTO damping coefficient, this study neglects the effect of hydrodynamic interactions in the time-domain analysis.

3.4. Damping Correction

The viscosity significantly affects the dynamic responses of the combined structure, but the effect of viscous damping cannot be calculated based on potential flow theory. To ensure the accuracy of WEC power calculations, it is necessary to correct the buoy's heave motion damping for viscous effects. This paper uses empirical formulas to calculate the viscosity damping. First, the critical damping for the buoy's heave motion is calculated as follows [31]:

$$D_{critical} = 2\sqrt{(M_{33} + m_{33})K_{33}} \tag{5}$$

where M_{33} is the mass of the buoy, m_{33} is the added mass of the buoy at its natural frequency in heave motion, K_{33} denotes the hydrostatic stiffness in the heave direction. Based on reference [34], 8% of critical damping in the heave direction is recommended to be the viscosity damping.

3.5. PTO System

In this paper, the PTO system is modeled as a spring-damper system in AQWA, which consists of a linear spring with a stiffness coefficient K_{PTO} and an ideal damper with a damping coefficient B_{PTO} . The instantaneous output power of the WEC can be calculated based on the damping coefficient and the relative velocity between the buoy and the platform, as given by the following equation [18]:

$$P_{PTO} = B_{PTO}\dot{x}_{rel}^2(t) \tag{6}$$

where \dot{x}_{rel} is the relative velocity in heave motion between the torus-shaped buoy and the platform.

To calculate the average output power, the relative velocity between the WEC and column and damping coefficient have important roles. It can be is determined as

$$\bar{P}_{PTO} = \frac{1}{t} \int_0^t B_{PTO}\dot{x}_{rel}^2(t)dt \tag{7}$$

where t refers to the total considered time.

3.6. Verification of the Coupled Model

3.6.1. Offshore Floating Wind Turbine Model

To verify the accuracy of the wind turbine modeling within the numerical model, the results from F2A are compared with those from OpenFAST. Given that this study

focuses on a semi-submersible wind turbine, time-domain simulations are performed on the OC4-Deepcwind semi-submersible turbine model. Both methods employed the same pitch controller and identical wind fields generated by Turbsim, with average wind speeds of 11.4 m/s and turbulence of 8% [30]. The regular waves are characterized by a wave height (H) of 2 m and a period of 5 s. Figure 7 compares the rotor speed and rotor thrust computed by both OpenFAST and F2A, two parameters that significantly influence the wind turbine’s power output and platform dynamic response. It is evident that although there are slight discrepancies at the turning points between the two methods, the overall trends and amplitudes are basically consistent throughout the simulation.

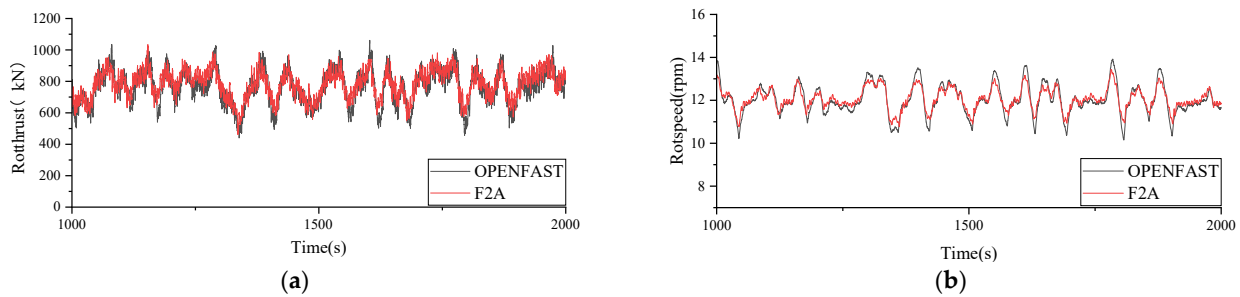


Figure 7. Comparison of rotor speed and rotor thrust (a) rotor thrust; (b) rotor speed.

3.6.2. Platform and Mooring Model

To validate the accuracy of the platform and mooring system modeling presented in this study, a steady-state analysis of the system is conducted. Detailed design parameters of a single mooring line are presented in Table 3. The coordinates of the anchors and fairleads can be found in [29].

There are six degrees of freedom rigid-body motions to the floating platform under marine conditions [35]. The natural periods of the platform across its six degrees of freedom are calculated. The results are compared with those computed by Luan et al. as displayed in Table 4 [29]. The results align closely, with the maximum discrepancy not exceeding 2%. The primary reason for this deviation might be the omission of the ballast water effects in our model, which affects an accurate representation of the mass distribution of the platform.

Table 4. Natural periods of the six degrees of freedom rigid-body motions of the 5-MW-CSC.

Freedom	Reflex	AQWA	Deviation
Surge	79.5 s	77.7 s	2.0%
Sway	79.5 s	77.7 s	2.0%
Heave	25.8 s	25.7 s	0.2%
Pitch	31.3 s	31.5 s	0.8%
Roll	31.3 s	31.5 s	0.7%
Yaw	58.1 s	57.7 s	0.6%

3.6.3. WEC Mode

In order to understand the performance of WEC in WWEC, Ren et al. conducted experimental research on the combined system of a monopile wind turbine and a torus-shaped WEC [27]. To validate the accuracy of the WEC model, this paper neglects the effect of rotor thrust on the monopile and establishes a numerical model in AQWA based on the wind–wave energy converter designed in the literature. The mean power of the WEC is calculated and then compared with the experimental results in the regular wave, as illustrated in Figure 8. The wave height of the regular waves is 2 m. The average error between the numerical model results and the experimental data is 15%. As the wave periods increase, the simulation results gradually align with the experimental data. The discrepancy might be attributed to the potential flow theory’s inability to account for fluid viscosity. The model relies on empirical formulas to introduce additional damping as a

simplified representation of viscosity effects, which still presents some differences from the experimental outcomes.

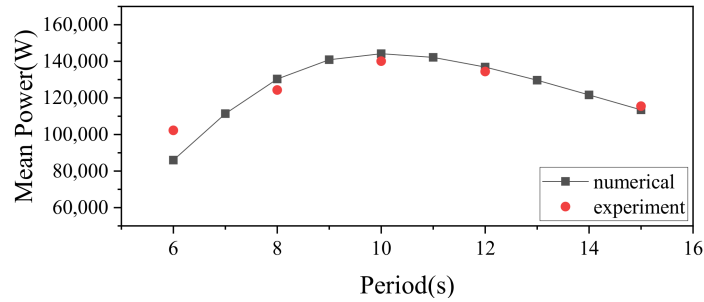


Figure 8. Comparison of mean power between numerical results and experimental data (H = 2 m).

4. Control Strategy of Mass-Adjustable Buoy Design

4.1. B_{PTO} Determined

To analyze whether the optimal damping coefficient of the WEC is influenced by variations in the buoy’s draft, this study evaluated the power output of the buoy at three different drafts. The range of the damping coefficient is from 1000 kNs/m to 2500 kNs/m, with a step size of 500. Wave amplitude is 1 m, with wave periods ranging from 7 s to 13 s. A turbulent wind field with an average wind speed of 11.4 m/s and a turbulence intensity of 8% is utilized as the input for calculations. The results are presented in Figure 9.

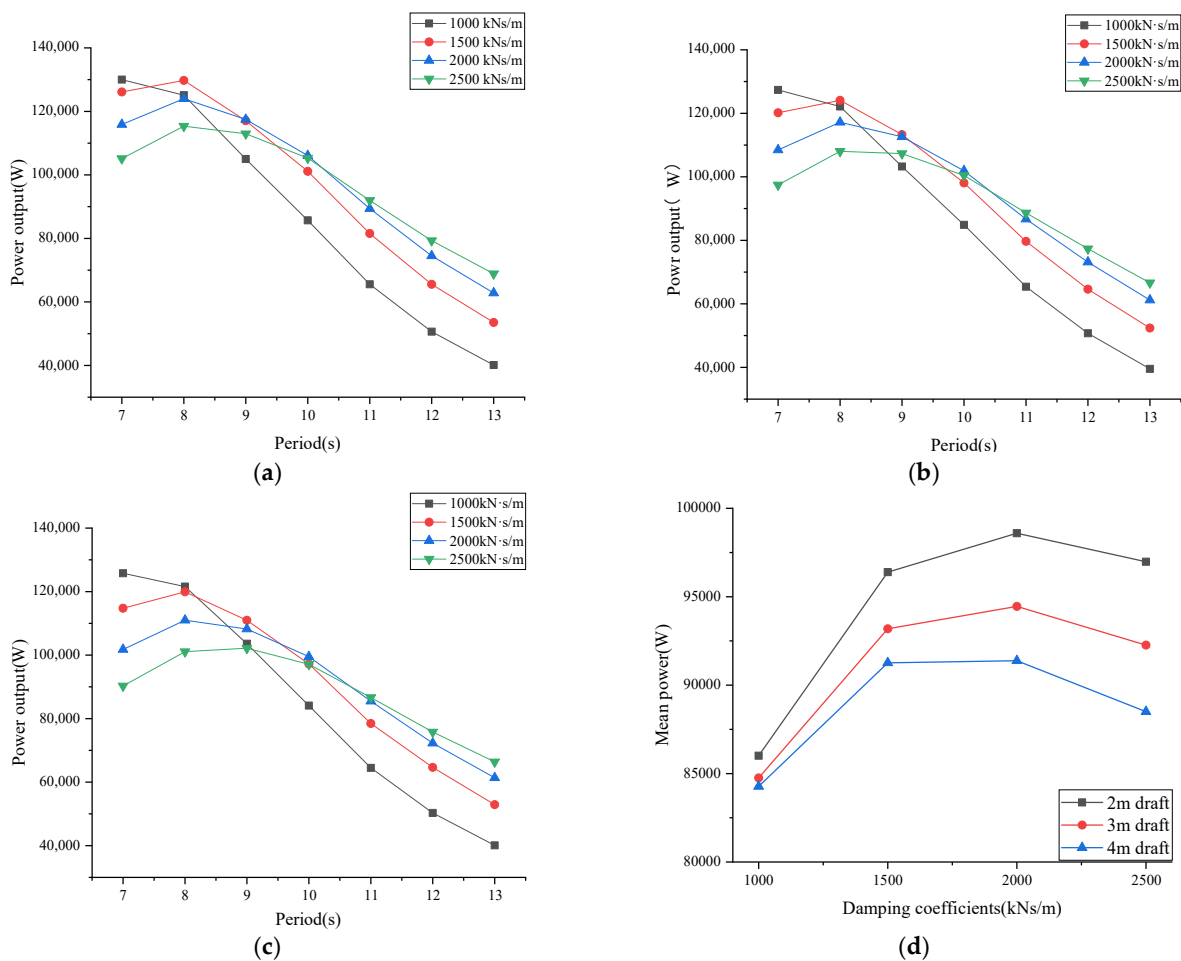


Figure 9. Power output of buoys with different masses for different PTO damping coefficients (a) draft = 2 m; (b) draft = 3 m; (c) draft = 4 m; (d) mean power.

Observations from the results for the buoy with a 2 m draft indicate that a larger damping coefficient results in better performance of the buoy under conditions of larger periods, while a smaller damping coefficient leads to better performance of the buoy under conditions of smaller periods. Different mass buoys exhibit consistent trends in power output as the damping coefficient varies. Calculating the mean power for the three buoys across the entire evaluation range reveals that the mean power rises with increasing damping coefficient, and the peak is all around 2000 kNs/m. It is posited that the optimal system damping coefficient remains unchanged while the buoy mass changes within the scope of this paper’s design. Consequently, the preliminary optimal system damping coefficient is determined to be 2000 kNs/m.

4.2. Control Strategy

Under the same wave conditions, there is little difference in the F-K force exerted by the waves on the bottom of the buoys with different drafts if the system is running properly. The difference in their power output is because a buoy with less mass moves faster, allowing more kinetic energy to be converted into electrical energy. However, having a smaller buoy mass is not always advantageous, as buoys with shallower draft are prone to demonstrate the phenomenon of water exit and water entry. Frequent occurrences of the phenomenon by the buoys can pose a threat to the stability of the system. To ensure the stability of the WWEC, restrictions need to be imposed on the WEC in extreme conditions.

Whether the buoy is out of the water surface can be determined by observing the F-K forces acting on the bottom of buoys. Taking the example of two buoys, with a wave period of 10 s. As shown in Figure 10, under the influence of regular waves with a 1 m wave amplitude, the F-K forces experienced by buoys are essentially consistent. As the wave amplitude increases, in the case of a 2 m wave amplitude, during the downward motion of the 1 m draft buoy, there are moments when the wetted surface area at the bottom significantly decreases, causing the shape of the F-K force versus time curve to undergo a transformation. There is no change for the shape of F-K force curve of the 2 m draft buoy compare to 1 m buoy. When the wave amplitude reaches 3m, there are moments when the F-K force equals zero for a 2 m draft buoy, indicating that the buoy is completely out of the water surface. If the wave amplitude continues to increase, the F-K force curve of 2 m draft buoy also undergoes a noticeable change.

When incident waves are regular waves, the output power of the buoy is the mean power of the buoy over one wave period. The power output of the two buoys is shown in Table 5. At lower wave amplitudes, the power output of the two buoys is nearly identical. As the wave amplitude increases, the 1 m draft buoy transitions from having a partially wetted surface to being out of the water surface at some moments. When the wave amplitude rises, the duration of the buoy being out of the water increases, resulting in a more significant power decrease. It can be observed that if the buoy experiences the phenomenon of being out of the water, the ability to capture wave energy will significantly decrease.

Table 5. Power output of two buoys in different wave amplitude (T = 10 s).

Amplitude	1 m	2 m	3 m	4 m
1 m draft buoy	104,100 W	328,670 W	473,368 W	519,696 W
2 m draft buoy	106,073 W	421,228 W	881,052 W	1,357,678 W

To determine the wave conditions suitable for buoys with various drafts, this paper calculates the power output of different buoys. The wave period is set from 5 s to 15 s, with wave amplitudes ranging from 1 m to 4 m, using a step increment of 1. The power output for buoys with different drafts is computed in regular waves. Due to the finite amplitude wave theory, when the wave steepness exceeds 1/7, wave breaking occurs, preventing the formation of complete waves. Thus, for waves with a period of 5 s under deep water

conditions, the amplitude cannot exceed 2.7 m. Only amplitudes of 1–2 m are considered, with the results shown in Figure 11.

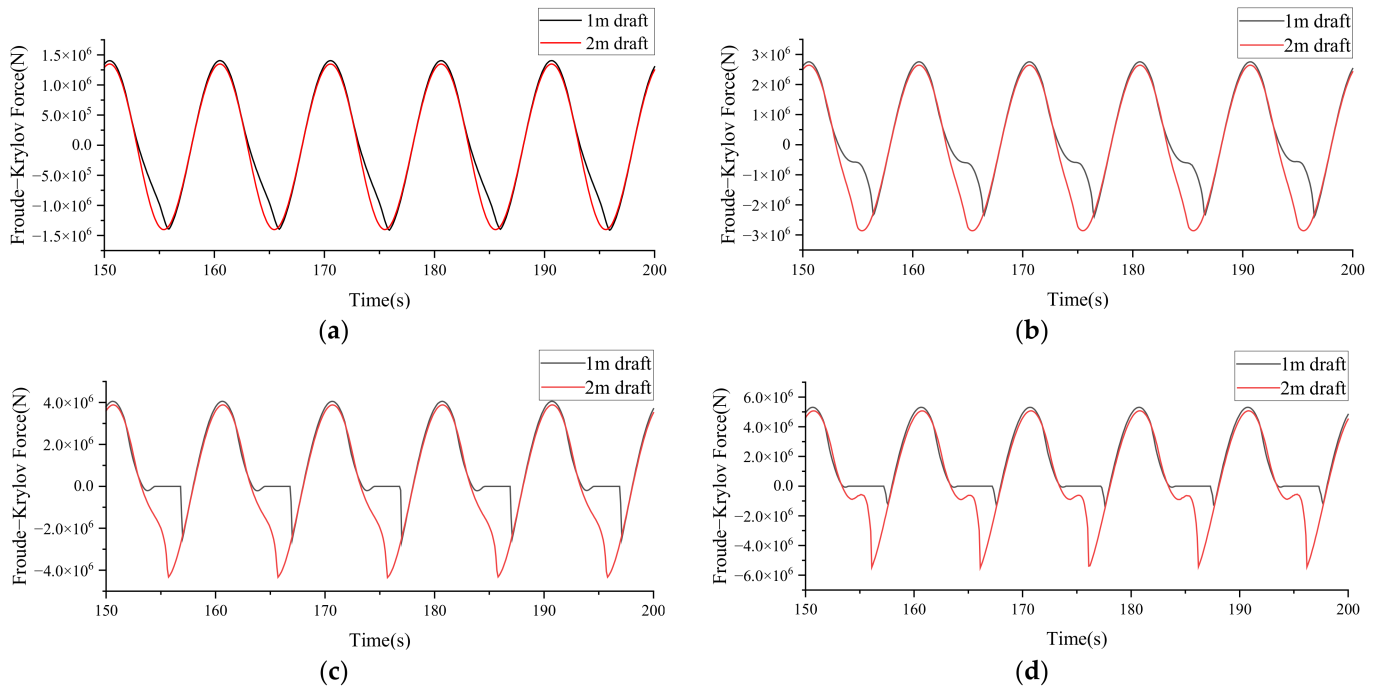


Figure 10. Comparison of F–K force for buoys between 1 m draft and 2 m draft. (a) Amplitude = 1 m; (b) amplitude = 2 m; (c) amplitude = 3 m; (d) amplitude = 4 m.

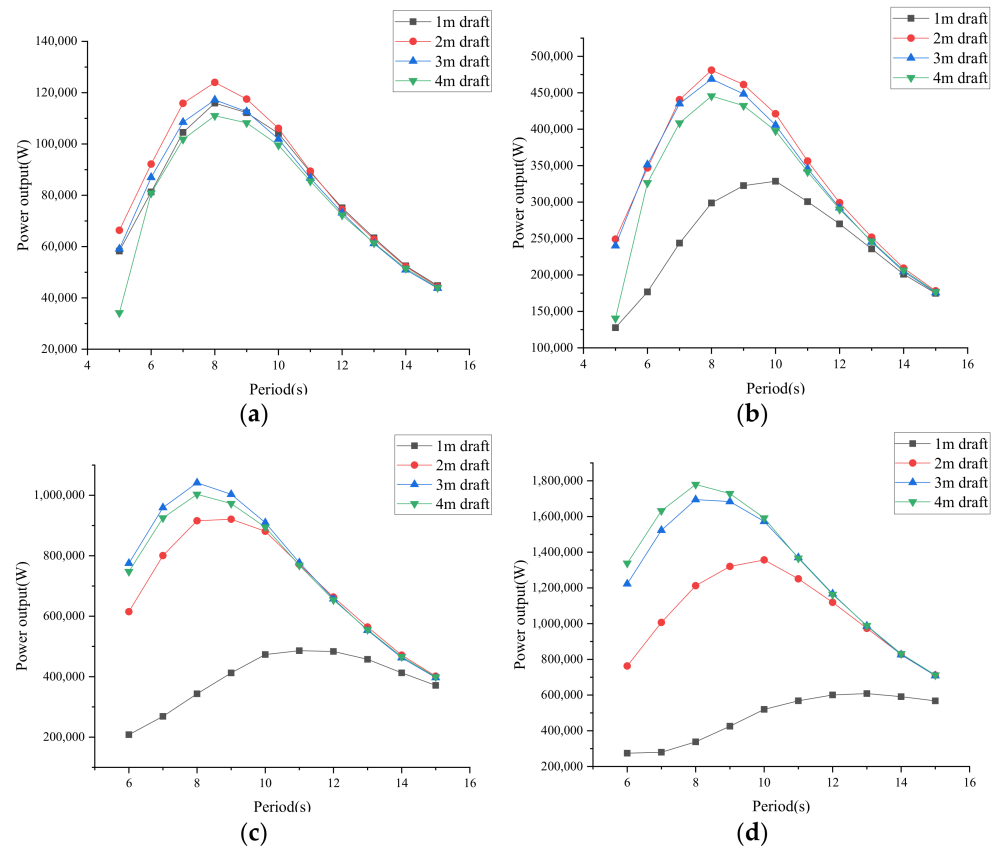


Figure 11. Comparison of power output between buoys with different draft in regular wave (a) amplitude = 1 m, (b) amplitude = 2 m, (c) amplitude = 3 m, (d) amplitude = 4 m.

At lower wave amplitudes, the buoy with a 2 m draft consistently exhibits the highest power output across the entire period range. This distinction is particularly evident when the period is less than 10 s, but the performance difference between buoys is negligible under the wave with long periods. With increasing wave amplitude, there emerges a pronounced difference between the 1m draft buoy and the others.

When the amplitude reaches 2 m, the gap between the 2 m and 3 m draft buoys narrows. When the amplitude reaches 3 m, the energy absorption capability of the 3 m draft buoy surpasses that of the 2 m draft buoy. As the wave amplitude increases, buoys with a deeper draft gradually gain an advantage. Until the amplitude rises to 4 m, the buoy with a 4 m draft demonstrates superior performance in most of the period range. When the amplitude is equal to 4 m and $T = 10$ s, the power output of 2 m draft buoy is 17.3% lower than that of 4 m draft buoy. Even without the occurrence of the water exit phenomenon, the impact of the F-K force variation on the output power of the buoy is evident. As the period lengthens, the difference in output power between the two buoys diminishes. This is because with longer wavelengths, the wave steepness decreases, which improves the reduction in wetted surface area at the bottom of the buoy. The F-K force exerted on different buoys are basically identical. It can be observed that the main reason for the variation in the buoy with the highest power output is the change in wave amplitude, and the period change only impacts the power gap of different buoys.

The mean power of each buoy under different wave amplitude conditions throughout the entire period range is calculated as shown in Figure 12. The curves of the 2 m draft buoy and the 3 m draft buoy intersect at a wave amplitude of 2.23 m, and the curves of the 3 m draft buoy and the 4 m draft buoy intersect at a wave amplitude of 3.28 m.

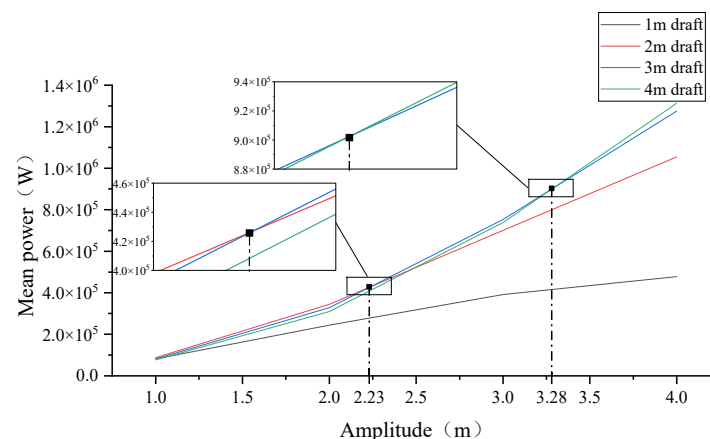


Figure 12. Comparison of mean power between buoys in different amplitudes.

This paper designs a mass adjustment strategy based on the performance of the buoy in regular waves. Considering that the wave height is equal to twice the wave amplitude, thresholds of 4.46 m and 6.56 m are set as the criteria for adjusting buoy mass. When H_s is less than 4.46 m, the draft of the buoy is adjusted to 2 m. When $4.46 \text{ m} < H_s < 6.56 \text{ m}$, the draft is adjusted to 3 m. When H_s is greater than 6.56 m, the draft is adjusted to 4 m. However, the significant wave height is obtained by calculating the average height of large waves in short-term sea conditions, which may differ from the wave height in regular waves. The peak period of irregular waves may also have a different impact on the system’s power output compared to the period of regular waves. The effectiveness of the adjustment strategy will be further discussed in the next part.

4.3. Validation

4.3.1. Stability Analysis

The healing moments come from aerodynamic loads on the rotor, tower, and platform and make the floating wind turbine rotate with respect to an axis in the water plane area. To ensure platform stability, the criterion specified in DNV-OS-J103 [36] is utilized to check the

intact stability and the damaged stability of the WWEC. The healing moment is calculated based on the aerodynamic load under the operational condition with 11.4 m/s mean wind speed. The results are shown in Figure 13.

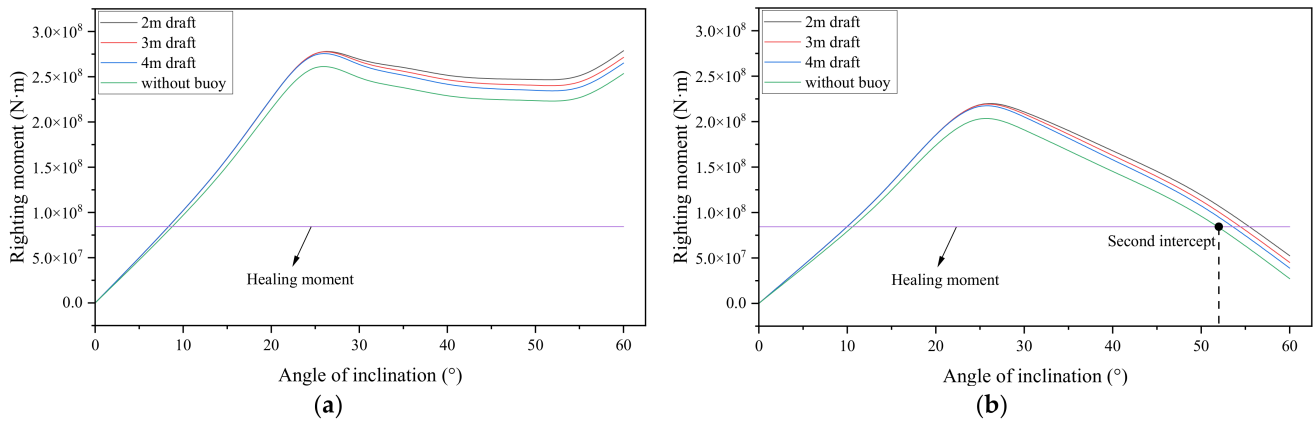


Figure 13. Righting moment and wind heeling moment curves (a) intact stability, (b) damaged stability.

It can be observed that compared to a normal floating wind turbine, a mass-adjustable buoy can increase the platform’s righting moment. Additionally, the smaller the mass of the buoy, the greater the platform’s righting moment. Therefore, it is only necessary to verify the stability of the floating wind turbine without buoys. As shown in Figure 13a, the righting moment curve and the righting moment curve do not have a second intersection point due to the mooring system, which ensures intact stability. As shown in Figure 13b, the stability under damage is assessed by assuming the failure of the mooring system. For column-stabilized units, the area under the righting moment curve to the angle of downflooding shall be greater than 130% of the area under the heeling moment curve to the same limiting angle [36]. The ratio of the area under the righting moment curve from 0 degrees to the second intersection to the corresponding area under the healing moment curve is 1.53, which is larger than 1.3.

4.3.2. Control Strategy Validation

To validate the feasibility of the designed, eight environmental conditions (ECs), as shown in Table 6 [37], were selected for testing. Turbulent wind fields are generated using TurbSim, and irregular waves are generated using the JONSWAP spectrum, for which the spectral peak enhancement factor γ is 3.3. EC1-6 represents normal operating conditions, while EC7 and EC8 represent extreme conditions where the average wind speed exceeds the turbine cut-out speed, resulting in the turbine ceasing operation. Under the environmental conditions of EC8, to ensure the safety of the system, the normal wave energy converter would cease operation, and the torus-shaped buoy would be submerged in water to prevent impact loads caused by the phenomenon of water exit and water entry. It is obvious that the significant wave height (H_s) in EC8 is far above 6.56 m. By evaluating the system’s performance under EC8, it can be determined whether further increasing the buoy’s mass is necessary under extreme conditions.

According to the defined ECs, the numerical model established in the previous sections is used for time-domain simulation, with a simulation duration of 4000 s. For removing startup effects, results are extracted after 1000 s. The power output of WECs under different conditions is calculated using Equation (7). The time of water exit corresponds to the time when the F-K force acting on the buoy is equal to zero.

The results are shown in Figure 14. For ECs 1–4, the 2 m draft buoy exhibited the highest mean power, while for ECs 5 and 6, the 3 m draft buoy showed the highest power output. In ECs 7 and 8, the 4 m draft buoy demonstrated the highest average power, consistent with the results obtained from the previously designed active control strategy. Comparing the time of water exit, it is observed that in conditions with low wave heights

(EC1-5), the phenomenon of water exit did not occur, and there are small differences in power output among different buoys. As the wave height increased, the 2 m and 3 m draft buoys exhibited an obvious phenomenon of water exit. The time of water exit for a 2 m draft buoy reached a time of 239.9 s in EC8, and the power difference between buoys reached up to 19.3% (comparison between 2 m draft buoy and 4 m draft buoy in EC8).

Table 6. Environment Conditions.

Case	H_s [m]	T_p [s]	U_w [m/s]	Turbulence Intension
EC1	2.10	9.74	5	22.4%
EC2	2.88	9.98	10	15.7%
EC3	3.20	10.11	12	14.6%
EC4	3.97	10.44	16	13.2%
EC5	4.80	10.82	20	12.4%
EC6	5.69	11.23	24	11.8%
EC7	9.77	12.95	40	11.0%
EC8	13.50	15.00	40	11.0%

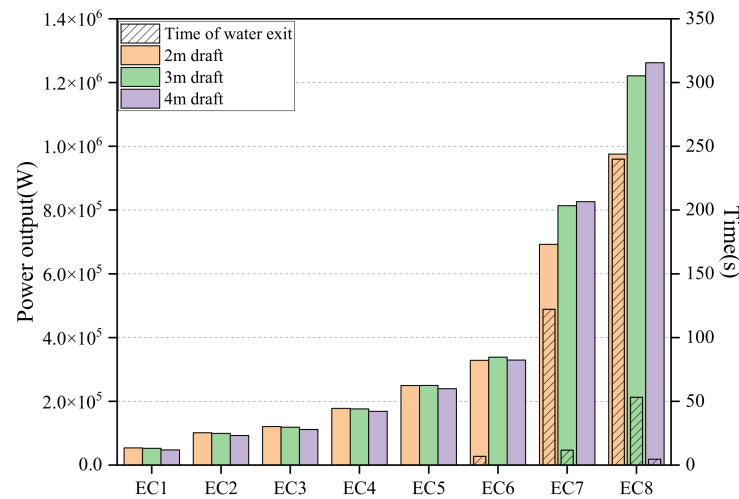


Figure 14. The power output and time of water exit for different mass buoys in ECs1–8.

Under the extreme conditions of EC8, the time of water exit for a 4 m draft buoy only reached 4.6 s. Therefore, the 4 m draft buoy is sufficient to handle most environmental conditions, and further increasing buoy mass is unnecessary. In summary, the designed mass-adjustable buoy in this paper can effectively enhance the system’s ability to capture wave energy and prevent the occurrence of water-exit phenomena that may affect system stability.

For an WWEC, the wave energy converter design should consider the influence on the floating wind turbine’s power output and dynamic response. The following analysis investigates the impact of the adjustable mass buoy on the wind turbine under both normal and extreme conditions. In normal operating conditions, the focus is on how changes in buoy mass affect wind power output. Given that the pitch and heave motions of the platform more significantly impact the wind turbine’s power output, we analyze the effects of buoy mass variation on these motions.

As illustrated in Figure 15, taking EC3 as an example, it is observed that variations in buoy mass have a minor effect on the pitch motion of the platform but a more substantial impact on the heave motion.

Subsequently, the impact of platform motion on wind power output is analyzed as shown in Figure 16. It can be observed that, due to the regulatory effects of the turbine’s pitch control and the generator’s control, the variations in the platform’s surge motion have a few impacts on the value of wind power output. Considering the importance of

wind turbine power stability for grid integration of wind farms, the standard deviation of wind power output is calculated to be 485.92 kW and 484.46 kW, which are nearly identical. Therefore, the effect of buoy mass variation on wind power output can be considered negligible.

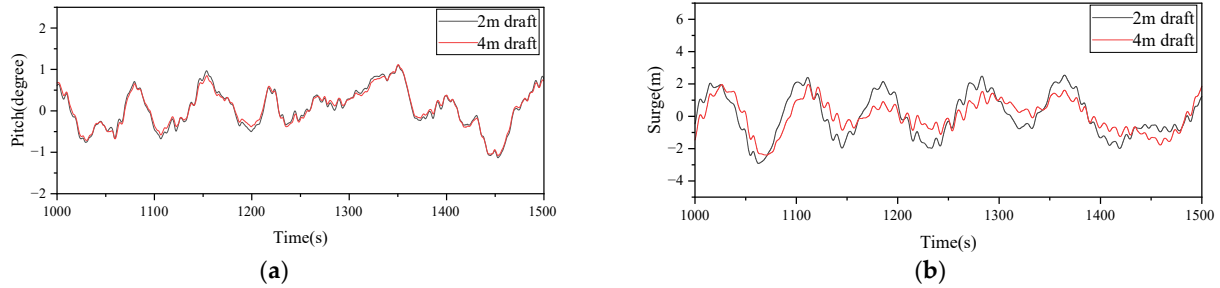


Figure 15. The impact of buoys on the dynamic response of the wind turbine in EC3 (a) pitch, (b) surge.

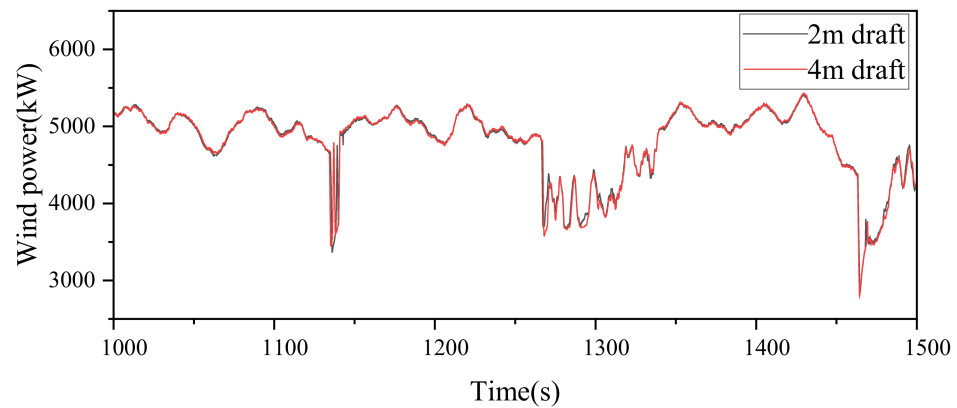


Figure 16. The output power of the wind turbine in EC3.

In extreme conditions, the wind turbine stops operating, the primary focus is on studying the impact of the mass-adjustable buoy on the mooring system. Conventional buoys for wind turbines are typically submerged and locked to ensure system stability. The wind-wave energy system designed in this study addresses the stability issues caused by slamming loads under extreme conditions. Further research is needed to investigate the impact of adjustable-mass buoys on the wind turbine system during operation under extreme conditions. In EC8, this study compares a conventional offshore floating wind turbine, a wind-wave energy system with the adjustable-mass buoy, and a normal wind-wave energy system that holds the buoy under the water. The dynamic responses of the wind turbine’s heave, pitch, and surge degrees of freedom are calculated. Then, the results are processed, as shown in Figure 17.

Comparing the dynamic responses in the surge and pitch directions of the wind turbine, it is evident that both the adjustable-mass buoy and the normal buoy have adverse effects on the motion of these two degrees of freedom. The average responses in the pitch motion increased by 23.9% and 14.7% compared to that of a wind turbine without a buoy, while the extreme values of the response increased by 18.9% and 8.8%. In the surge motion, the average responses increased by 20.8% and 7.5% compared to that of a wind turbine without a buoy, and the extreme values of the response increased by 51.2% and 41.1%. It can be observed that the influence caused by the mass-adjustable buoy is more significant under extreme conditions.

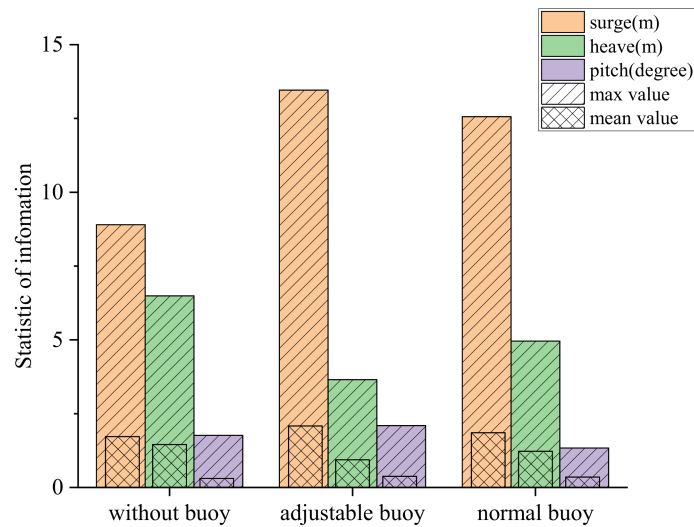


Figure 17. The mean power and time of water exit for different mass buoys in ECs1–8.

The power spectral density of tension in mooring 1 and mooring 2 is calculated as shown in Figure 18. It is evident that the mooring loads are divided into high- and low-frequency bands. The high-frequency band is controlled by wave loads, while the low-frequency band is dominated by wind loads. Under extreme conditions, due to the pitch control, the wind load significantly decreases, thus the mooring system load is primarily governed by wave loads. Wave loads mainly affect the platform’s heave and surge motion responses.

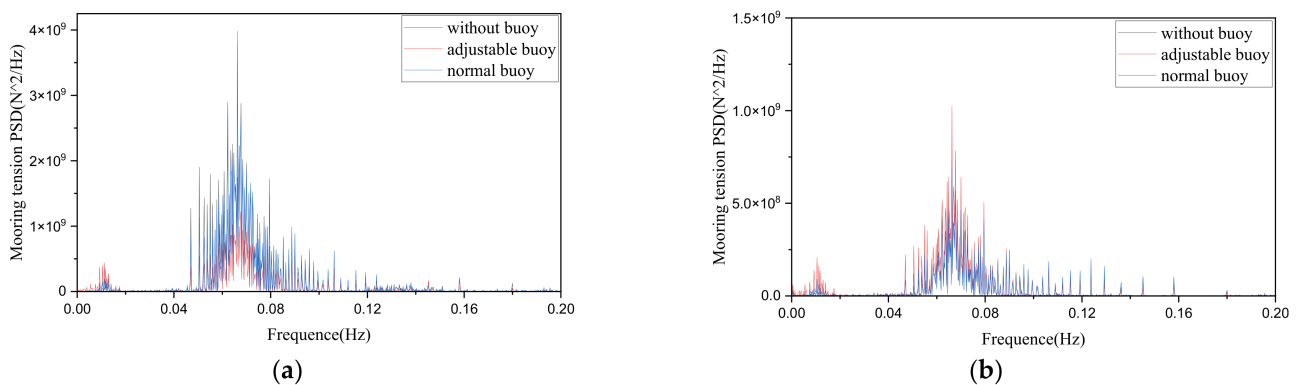


Figure 18. The power spectral density (PSD) of the loads on the mooring system; (a) mooring 1 (b) mooring 2.

As illustrated in Figure 18a, it can be observed that for mooring line 1, the system with the mass-adjustable buoy experiences the least tension load. This is because mooring 1 is most affected by the platform’s heave motion, and the adjustable mass buoy can significantly reduce the platform’s heave motion. In Figure 18b, it is shown that, compared to the other two systems, mooring 2 in the system with the adjustable mass buoy experiences the highest load. This is because mooring 2 and 3 are more influenced by the platform’s surge motion. Comparing the load spectra of mooring 1 and mooring 2, it is evident that mooring 1 experience significantly more load pressure than mooring 2 and 3. Therefore, a mass-adjustable buoy can reduce the load on mooring 1 under extreme conditions, which is more beneficial for reducing survival pressure on the mooring system and maintaining system stability.

5. Conclusions

This paper proposes a novel WWEC with a mass-adjustable buoy, which effectively enhances the capability to capture wave energy. To design the mass-adjustable buoy, a coupled numerical model is established to determine the mass adjustment strategy and then validate the effectiveness and feasibility of the mass-adjustable buoy. The main conclusions are summarized as follows:

- (1) The mass adjustment mechanism was designed based on the shape of the buoy and the connection between the buoy and the platform. The mechanism adjusts the buoy's mass by varying the capacity of the ballast water.
- (2) The optimal damping coefficient of the PTO system is not affected by the change in the buoy's mass. When the damping coefficient is 2000 kNs/m, the buoy exhibits the strongest capability to absorb wave energy.
- (3) A buoy with a smaller mass experiences lower kinetic energy losses, resulting in higher power output. As the wave amplitude increases, it is easier for the smaller mass buoy to move out of the water, which leads to a significant decrease in power output.
- (4) Compared to normal buoys, the mass-adjustable buoy enhances power output by up to 19.3% and significantly reduces the time of water exit of the buoy, thereby mitigating the impact of slamming loads on system stability.
- (5) Under extreme conditions (EC8), installing the adjustable-mass buoy can reduce the maximum heave response of the wind turbine by 43.8% and decrease the mean amplitude by 35.7%. Moreover, it can reduce survival pressure on the mooring system and maintaining system stability.

In summary, this paper proposes a design method for a novel WWEC with a mass-adjustable buoy. An adjustment strategy is proposed to achieve WWEC stability and power optimization. This design demonstrates significant development potential, which can be integrated into more studies based on the selection of different platform types and adjustments in the number of buoys. The conceptual design of the mass-adjustable buoy also has limitations. Due to the lack of experimental conditions, it is hard to further validate the design of the WWEC. The buoy structure also has some deficiencies that require further optimization; once submersed, the upper surface in water will affect the adjustment of the mass.

Author Contributions: Conceptualization, Y.S.; methodology, Y.S.; software, Y.S.; validation, Y.S., J.L. and J.Z.; investigation, Z.Z.; data curation, Y.S.; writing—original draft preparation, Y.S.; writing—review and editing, Y.S., R.Z. and J.Z.; supervision, J.Z.; funding acquisition, J.Z. All authors have read and agreed to the published version of the manuscript.

Funding: The authors are thankful to the supported by Fuzhou Institute of Oceanography, grant 2024F05.

Institutional Review Board Statement: Not applicable.

Informed Consent Statement: Not applicable.

Data Availability Statement: The original contributions presented in the study are included in the article, further inquiries can be directed to the corresponding authors.

Conflicts of Interest: The authors declare no conflicts of interest.

References

1. Zhang, Y.; Li, D.; Hong, S.; Zhang, M. Design of a new oscillating-buoy type wave energy converter and numerical study on its hydrodynamic performance. *Brodogr. Int. J. Nav. Archit. Ocean. Eng. Res. Dev.* **2023**, *74*, 145–168. [[CrossRef](#)]
2. Legaz, M.J.; Soares, C.G. Evaluation of various wave energy converters in the bay of Cádiz. *Brodogr. Int. J. Nav. Archit. Ocean. Eng. Res. Dev.* **2022**, *73*, 57–88. [[CrossRef](#)]
3. Global Wind Energy Council. GWEC Global Wind Report 2023. 2023. Available online: <https://gwec.net/globalwindreport2023/> (accessed on 20 August 2024).
4. Peiffer, A.; Roddier, D.; Aubault, A. Design of a point absorber inside the WindFloat structure. In Proceedings of the International Conference on Offshore Mechanics and Arctic Engineering, Rotterdam, The Netherlands, 19–24 June 2011; pp. 247–255.

5. Bachynski, E.E.; Moan, T. Point Absorber Design for a Combined Wind and Wave Energy Converter on a Tension-Leg Support Structure. In Proceedings of the ASME 2013 32nd International Conference on Ocean, Offshore and Arctic Engineering, Nantes, France, 9–14 June 2013.
6. Michailides, C.; Luan, C.; Gao, Z.; Moan, T. Effect of flap type wave energy converters on the response of a semi-submersible wind turbine in operational conditions. In Proceedings of the International Conference on Offshore Mechanics and Arctic Engineering, San Francisco, CA, USA, 8–13 June 2014; p. V09BT09A014.
7. Li, L.; Gao, Y.; Yuan, Z.; Day, S.; Hu, Z. Dynamic response and power production of a floating integrated wind, wave and tidal energy system. *Renew. Energy* **2018**, *116*, 412–422. [[CrossRef](#)]
8. Sarmiento, J.; Iturrioz, A.; Ayllón, V.; Guanche, R.; Losada, I. Experimental modelling of a multi-use floating platform for wave and wind energy harvesting. *Ocean. Eng.* **2019**, *173*, 761–773. [[CrossRef](#)]
9. Wan, L.; Ren, N.; Zhang, P. Numerical investigation on the dynamic responses of three integrated concepts of offshore wind and wave energy converter. *Ocean. Eng.* **2020**, *217*, 107896. [[CrossRef](#)]
10. Gubesch, E.; Sergiienko, N.Y.; Nader, J.-R.; Ding, B.; Cazzolato, B.; Penesis, I.; Li, Y. Experimental investigation of a co-located wind and wave energy system in regular waves. *Renew. Energy* **2023**, *219*, 119520. [[CrossRef](#)]
11. Farkas, A.; Degiuli, N.; Martić, I. Assessment of offshore wave energy potential in the Croatian part of the Adriatic Sea and comparison with wind energy potential. *Energies* **2019**, *12*, 2357. [[CrossRef](#)]
12. Muliawan, M.J.; Karimirad, M.; Moan, T.; Gao, Z. STC (Spar-Torus Combination): A Combined Spar-Type Floating Wind Turbine and Large Point Absorber Floating Wave Energy Converter—Promising and Challenging. In Proceedings of the International Conference on Offshore Mechanics and Arctic Engineering, Rio de Janeiro, Brazil, 1–6 July 2012.
13. Li, Y.; Ong, M.C.; Wang, K.; Li, L.; Cheng, Z. Power performance and dynamic responses of an integrated system with a semi-submersible wind turbine and four torus-shaped wave energy converters. *Ocean. Eng.* **2022**, *259*, 111810. [[CrossRef](#)]
14. Michailides, C.; Gao, Z.; Moan, T. Experimental study of the functionality of a semisubmersible wind turbine combined with flap-type Wave Energy Converters. *Renew. Energy* **2016**, *93*, 675–690. [[CrossRef](#)]
15. Da Silva, L.S.P.; Sergiienko, N.Y.; Cazzolato, B.; Ding, B. Dynamics of hybrid offshore renewable energy platforms: Heaving point absorbers connected to a semi-submersible floating offshore wind turbine. *Renew. Energy* **2022**, *199*, 1424–1439. [[CrossRef](#)]
16. Homayoun, E.; Ghassemi, H.; Ghafari, H. Power performance of the combined monopile wind turbine and floating buoy with heave-type wave energy converter. *Pol. Marit. Res.* **2019**, *26*, 107–114. [[CrossRef](#)]
17. Haji, M.N.; Kluger, J.M.; Sapsis, T.P.; Slocum, A.H. A symbiotic approach to the design of offshore wind turbines with other energy harvesting systems. *Ocean. Eng.* **2018**, *169*, 673–681. [[CrossRef](#)]
18. Homayoun, E.; Panahi, S.; Ghassemi, H.; He, G.; Liu, P. Power absorption of combined wind turbine and wave energy converter mounted on braceless floating platform. *Ocean. Eng.* **2022**, *266*, 113027. [[CrossRef](#)]
19. Liu, C.; Yang, Q.; Bao, G. Latching control using optimal control method for a raft-type wave energy converter. *Ships Offshore Struct.* **2018**, *13*, 138–154. [[CrossRef](#)]
20. Hillis, A.J.; Whitlam, C.; Brask, A.; Chapman, J.; Plummer, A.R. Active control for multi-degree-of-freedom wave energy converters with load limiting. *Renew. Energy* **2020**, *159*, 1177–1187. [[CrossRef](#)]
21. Fang, H.; Jin, L. Investigation on resonance response of mass-adjustable float in wave energy conversion system. *Energy Procedia* **2019**, *158*, 315–320. [[CrossRef](#)]
22. Martić, I.; Degiuli, N.; Grlj, C.G. Scaling of wave energy converters for optimum performance in the Adriatic Sea. *Energy* **2024**, *294*, 130922. [[CrossRef](#)]
23. Men, J.; Yan, F.; Wang, Y.; Wang, L.; Zheng, X.; Wang, W. An evaluation of mooring system in a wind-wave hybrid system under intact and accident states. *Ocean. Eng.* **2023**, *283*, 115071. [[CrossRef](#)]
24. Wan, L.; Gao, Z.; Moan, T. Model test of the STC concept in survival modes. In Proceedings of the International Conference on Offshore Mechanics and Arctic Engineering, San Francisco, CA, USA, 8–13 June 2014.
25. Wan, L.; Gao, Z.; Moan, T. Experimental and numerical study of hydrodynamic responses of a combined wind and wave energy converter concept in survival modes. *Coast. Eng.* **2015**, *104*, 151–169. [[CrossRef](#)]
26. Wan, L.; Gao, Z.; Moan, T.; Lugni, C. Comparative experimental study of the survivability of a combined wind and wave energy converter in two testing facilities. *Ocean. Eng.* **2016**, *111*, 82–94. [[CrossRef](#)]
27. Ren, N.; Ma, Z.; Fan, T.; Zhai, G.; Ou, J. Experimental and numerical study of hydrodynamic responses of a new combined monopile wind turbine and a heave-type wave energy converter under typical operational conditions. *Ocean. Eng.* **2018**, *159*, 1–8. [[CrossRef](#)]
28. Jonkman, J.; Butterfield, S.; Musial, W.; Scott, G. *Definition of a 5-MW Reference Wind Turbine for Offshore System Development*; National Renewable Energy Lab. (NREL): Golden, CO, USA, 2009.
29. Luan, C.; Gao, Z.; Moan, T. Design and analysis of a braceless steel 5-mw semi-submersible wind turbine. In Proceedings of the International Conference on Offshore Mechanics and Arctic Engineering, Busan, Republic of Korea, 18–24 June 2016.
30. Yang, Y.; Bashir, M.; Michailides, C.; Li, C.; Wang, J. Development and application of an aero-hydro-servo-elastic coupling framework for analysis of floating offshore wind turbines. *Renew. Energy* **2020**, *161*, 606–625. [[CrossRef](#)]
31. Gao, W.; Dong, L.; Huang, J. ANSYS AQWA Software Introduction and Improvement. In *China Water Resour*; Hydropower Press: Beijing, China, 2018.

32. Lin, J.; Wang, Y.; Duan, H.; Zhang, J. Optimization Design of Blades for a Scaled Offshore Floating Wind Turbine. In Proceedings of the Advances in Mechanical Design, Changsha, China, 14–16 August 2022.
33. Jonkman, J.M.; Buhl, M.L., Jr. *Fast User's Guide-Updated August 2005*; National Renewable Energy Lab. (NREL): Golden, CO, USA, 2005.
34. Yapo, W.; Zhang, L.; Michailides, C.; Wan, L.; Shi, W. Hydrodynamic Response of a Combined Wind–Wave Marine Energy Structure. *J. Mar. Sci. Eng.* **2020**, *8*, 253. [[CrossRef](#)]
35. Lin, J.; Wang, Y.; Duan, H.; Liu, Y.; Zhang, J. A scaled wind turbine model-based aerodynamic testing apparatus for offshore floating wind turbines. *J. Mar. Eng. Technol.* **2023**, *22*, 263–272. [[CrossRef](#)]
36. *DNV-OS-J103*; Design of Floating Wind Turbine Structures. Offshore Standard DNV-OS-J103. DNV GL: Høvik, Norway, 2013.
37. Xu, K.; Zhang, M.; Shao, Y.; Gao, Z.; Moan, T. Effect of wave nonlinearity on fatigue damage and extreme responses of a semi-submersible floating wind turbine. *Appl. Ocean. Res.* **2019**, *91*, 101879. [[CrossRef](#)]

Disclaimer/Publisher's Note: The statements, opinions and data contained in all publications are solely those of the individual author(s) and contributor(s) and not of MDPI and/or the editor(s). MDPI and/or the editor(s) disclaim responsibility for any injury to people or property resulting from any ideas, methods, instructions or products referred to in the content.